Received: 14 September 2026 | Revised:16 November 2026 | Accepted: 18 November 2026

https://doi.org/10.56946/jce.v5i2.1087
Volume 5(2): 47-58

Journal of Chemistry and Environment

Research Article

Theoretical Insights into Optoelectronic and Thermoelectric Response of A_2LiAsI_6 (A = Na, K, Cs) Double Perovskite

Masaood Khan[1, †], Murad Khan[2, †], Khalid Khan[3], Muhammad Khurshid[4], Muhammad Jamshed[5*], Zama Jan[6*]

[1]Department of Physics, Abdul Wali Khan University Mardan 23200, Pakistan.
[2]Department of Chemical Engineering, Faculty of Mechanical, Chemical and Industrial Engineering, University of Engineering and Technology, Peshawar 25120, Pakistan.
[3]School of Mechanical and Electrical Engineering, University of Electronic Science and Technology of China, Chengdu, 611731, China.
[4]Materials Modeling and Simulation Lab, University of Science & Technology Bannu 28100, Department of Physics, Khyber Pakhtunkhwa, Pakistan.
[5]Hainan International Joint Research Center of Marine Advanced Photoelectric Functional Materials, College of Chemistry and Chemical Engineering, Hainan Normal University, Haikou, 571158, China.
[6]MOE Key Laboratory for Non-equilibrium Synthesis and Modulation of Condensed Matter, Shaanxi Province Key Laboratory of Advanced Functional Materials and Mesoscopic Physics, School of Physics, Xi'an Jiaotong University, Xi'an, Shaanxi 710049, China.

*Correspondence: Muhammad Jamshed (202509d003@hainnu.edu.cn), Zama Jan (zamaj2093@gmail.com)
[†]These authors contributed equally in this work.

Abstract

Lead-free halide double perovskites have emerged as promising semiconductor materials. Density functional theory (DFT) calculations were employed to investigate the structural, electronic, optical, elastic, and thermoelectric properties of lead-free halide double perovskites A_2LiAsI_6 (A = Na, K, Cs). All compounds are energetically and mechanically stable, with tolerance factors ranging from 0.903 to 1.027. Using Becke–Johnson (TB-mBJ) potential approach, an indirect semiconducting character is found with bandgap values of 1.330, 1.321, and 1.365 eV for Na_2LiAsI_6, K_2LiAsI_6 and Cs_2LiAsI_6, respectively. Strong absorption from the visible to ultraviolet range with a high dielectric response, excellent refractive indices and moderate reflectivity is revealed by optical experiments, suggesting effective light-harvesting capability. According to elastic analysis, each compound satisfies the Born stability criteria. Among the compounds, K_2LiAsI_6 exhibits superior stiffness and ductility, however, Na_2LiAsI_6 and Cs_2LiAsI_6 are comparatively softer and more brittle. In addition, Boltzmann transport calculations reveal that K_2LiAsI_6 and Cs_2LiAsI_6 exhibit high electrical conductivity and power factor, promising for thermoelectric applications.

Keywords: Lead free halide double perovskites, First-principal calculations, Optoelectronic and thermoelectric performance

1. Introduction

The demand for renewable energy sources has risen as conventional energy sources become scarcer. Researchers from all over the world are thoroughly examining alternative renewable energy sources to address the worsening global energy problem and the related environmental problems. To reduce reliance on traditional fossil fuels while maintaining economic viability, environmental preservation, and long-term energy security for next -generations, these sustainable energy solutions are being created [1, 2]. Solar energy is regarded as one of the most economical and ecologically beneficial of the ideal renewable energy technologies. Carefully choosing and designing appropriate materials for optoelectronic device applications is essential to increasing solar energy conversion efficiency since these materials have a direct impact on light absorption, charge transfer, and overall device performance [3-5]. Over the past decade, substantial developments have been made in perovskite technology, such as the use of photoluminescence (PL) for solar energy production [6-8]. Double perovskite (DP) can be significantly scaled up and has applications in solar cells [9], and optoelectronic devices [10, 11]. The inorganic cations have been substituted, enhancing thermal reliability. Furthermore, halide-based DPs have gained great attention for manufacturing solar energy technology and improve their conversion performance. The power conversion efficiency (PCE) has enhanced over the previous several years, ranging (3.8 % to 25.2 %). Todate, in case of multijunction thin film solar cells, the conversion rates reached to 47.1 % [12-14]. High-performance metal halide PDs require key material attributes, namely strong optical absorption, high charge carrier mobility, an appropriate direct bandgap, and a broad charge carrier diffusion range, which collectively dictate their optoelectronic performance.

Lead-free double perovskite halides have emerged as environmentally sustainable alternatives to their lead-based counterparts, with silver (Ag) and bismuth (Bi) serving as the principal substitutional elements in their compositional framework [15-18]. A promising strategy to circumvent the toxicity associated with lead involves the incorporation of a complex arrangement of trivalent and monovalent cations,

yielding compounds that conform to the general structural formula A_2XYH_6. Within this crystallographic framework, A denotes a large monovalent cation, such as sodium (Na^+), while X and Y correspond to monovalent and trivalent cations, respectively, and H represents either a halogen or oxygen anion occupying the anionic site. In a notable advancement within this domain, the indium-based halide DP $Cs_2InAgCl_6$ was successfully synthesized and comprehensively characterized [19]. Nevertheless, a significant proportion of these double perovskite compounds continue to exhibit considerable limitations, particularly with respect to poor optical quality and excessively wide bandgaps, which fundamentally restrict their viability and applicability in photovoltaic technologies.

Recently, various lead-based halide perovskites, for example, have established into sophisticated semiconductors for various optoelectronic applications, including photovoltaic in $CsPbBr_3$ [20]. Their establishment was only constrained in the presences of lead (Pb), which exhibit to be a toxic element in their chemical composition [21]. This limitation is reflected to be a primer steps restricting marketing. To overcome these challenges, lead free halide DPs materials are potential candidates to eliminated toxicity [22, 23], and proficient for optoelectronic and thermoelectric applications. Moreover, Murraza et al. examined the DPs $Rb_2AgTlCl_6$ and $Cs_2AgTlCl_6$, with highly stable and potential absorption [24]. However, the preparation of several halide-based perovskites, such as Cs_2BiAgI_6, $Cs_2InAgCl_6$, and $Cs_2BiAgBr_6$, exhibited that these materials are poor performance for solar applications because of their narrow optical properties and wide bandgaps [25-27]. The design of molecular architectures to create lightweight, easily synthesized hybrid perovskites has advanced significantly in recent research. However, because of their low stability and the poisonous nature of lead-based components, commonly investigated hybrid perovskites like $CH_3NH_3PbX_3$ (X = I, Cl, Br) have limits in solar energy applications [28-30]. Therefore, the advancement of next-generation perovskite-based solar energy applications depends on the development of stable, environmentally safer lead-free DPs [31]. Besides, a lot of research has been done to create ecologically safe lead-free halide perovskites by substituting non-toxic metal cations for lead. These materials are significant for solar cells and optoelectronic devices due to their promising optical characteristics, which include strong optical absorption, low reflection, and an appropriate band structure [21, 32, 33]. Thus, lead-free metal halide perovskites (ABX_3) continue to be intriguing options for optoelectronic applications despite possible structural instability. Similarly, because of their advantageous characteristics, the general formula of metal halide-based for DPs is $A_2BB'X_6$ are likewise seen as strong contenders for such applications [16, 34]. The chemical composition of materials forming interfaces has a significant impact on how stable working gadgets are, including DP compounds. Therefore, detailed investigations are necessary to understand the impact of ion migration on the long-term stability and performance of DP-based devices [26]. Because of their capacity to preserve a stable and advantageous crystal structure, which is controlled by the relative contributions and interactions of the constituent metal ions, halide DP are practically significant [35, 36]. Previous reports indicates that the DFT investigations of DPs employ a wide range of exchange-correlation functional [37, 38]. Although the material demonstrates thermal stability up to 700 K [16] .The absence of a direct bandgap restricts the applicability of $Cs_2BiAgBr_6$ perovskite in solar energy devices. Therefore, band structure engineering is required to induce a direct bandgap character in order to enhance its suitability for photovoltaic applications [17]. Recently, $Cs_2AgInCl_6$ DP has gained attention due to its ability to exhibit a tunable direct bandgap, indicating that optoelectronic applications could benefit from it [19]. This chemical has interesting properties for possible uses in solar energy harvesting and thermoelectric devices, according to both theoretical and experimental research [39]. In addition, investigated the structural, electrical, thermoelectric, and optical characteristics of Cs_2InAgX_6 (X = Cl, Br, I) using the GGA and TB-mBJ potential [40]. They used GGA and LDA approximations to examine the structural and optoelectronic characteristics of the direct band-gap DP $Cs_2AgInCl_6$, indicating its possible use in electrical devices [41]. Also examined the optical, electrical, and structural characteristics of Cs_2AgBiX_6 (X = Cl, Br, I) in the cubic phase. Additionally, they investigated the optoelectronic properties of Cs_2NaBX_6 (X = Cl, Br, I; B = Sb, Bi)[42].

Herein, we study electronic, optical, and thermoelectric properties of A_2LiAsI_6 (A = Na, K, Cs) DPs halides using first principles calculations. Our goal is to methodically adjust the electrical structure, including the bandgap and density of states, by changing the A-site cations (Na, K, and Cs) charge transport behavior, and optical response. The present study provides a comprehensive theoretical understanding of the structure and their property relationship of A_2LiAsI_6 DPs, potential candidates for optoelectronic and thermoelectric applications.

2. Computational details

DFT calculations are performed using full-potential linearized augmented plane wave (FP-LAPW) approach implemented in WIEN2k code [43]. The generalized gradient approximation (GGA) and TB-mBJ exchange-correlation potentials, are used to solve the Kohn-Sham equations [44]. Structure optimization includes determining ground-state appropriate ties utilizing the WIEN2k software [43]. The calculation was carried out as follows. First, the crystal unit cell was classified into non-overlapping muffin-tin (MT) spheres centered at the constituent atoms and an interstitial region. Second, inside the MT spheres, the wave functions were widened in radial functions multiplied by spherical harmonics up to $I_{max} = 10$, the wave functions in the interstitial region were represented by plane waves with $R_{MT}K_{max} = 7$. The Brillouin zone was sampled using a dense mesh of 1000 (k)-points under periodic boundary conditions. The resulting self-consistent electronic structure was subsequently used to investigate the structural, electronic, optical, elastic, and thermoelectric properties of the A_2LiAsI_6 (A = Na K Cs) double-perovskite compounds [45, 46]. Transport characteristics were computed using the Boltz Trap code interfaced with WIEN2k. The energy and force convergence criteria were set as 10^{-5} Ry and 0.04. The optical

properties of halide DPs A_2LiAsI_6 (A = Na, K, and Cs) can be described by their complex dielectric constant, represented by ε(ω). The two components of the dielectric constant are described by the Kramers-Kroning relations, as presented in equation (1) [47].

$$\varepsilon_1(\omega)=1+\frac{2}{\pi} p \int_0^{\infty} \frac{\omega \varepsilon_2(\omega)}{\omega'^2-\omega^2} d \quad (1)$$

$$\varepsilon_2(\omega) \frac{e^2\hbar}{\pi m^2\omega^2} \sum v, c \int BZ |M_{cv}(K)|^2 \delta [\omega_{cv}(K) - \omega] d^3k \quad (2)$$

Using the real and imaginary components, other optical characteristics are obtained and are expressed as:

$$L(\omega)=\frac{\varepsilon_1(\omega)}{\varepsilon_1^2(\omega)+\varepsilon_2^2(\omega)} \quad (3)$$

$$I(\omega)=\frac{\sqrt{2}\omega}{c}\left(\sqrt{(\varepsilon_1^2(\omega)\varepsilon_2^2(\omega)}-\varepsilon_1(\omega)\right)^{\frac{1}{2}} \quad (4)$$

$$n(\omega)=\left(\frac{1}{2}\left[\sqrt{\varepsilon_1^2(\omega)+\varepsilon_2^2(\omega)}+\epsilon_1(\omega)\right]\right)^{\frac{1}{2}} \quad (5)$$

$$R(\omega)=\left|\frac{\sqrt{\varepsilon(\omega)-1}}{\sqrt{\varepsilon(\omega)+1}}\right|^2 \quad (6)$$

Here in equation (1), $\varepsilon_1(\omega)$ and $\varepsilon_2(\omega)$ represent the real and imaginary parts of the complex dielectric function, respectively; ω indicates the angular frequency of the incident photon; ω′ denotes the integration variable; and p indicates the Cauchy principal value of the integral. In Equation (2), *e* represents the elementary charge; *h* indicates Planck's constant; *m* denotes the electron mass; *v* and *c* represent the valence and conduction bands, respectively; *BZ* indicates the Brillouin zone; $M_{cv}(K)$ denotes the momentum matrix element; *K* indicates the wave vector; and $\omega_{cv}(K)$ represents the energy difference between the conduction and valence bands. In Equation (3), L(ω) indicates the energy loss function. In Equation (4), I(ω) represent the absorption coefficient and *c* denotes the speed of light. In Equation (5), n(ω) indicates the refractive index. In Equation (6), R(ω) represents the reflectivity and $\varepsilon(\omega)$ denotes the complex dielectric function.

3. Result and discussion

3.1. Structural Properties

The structural stability of lead-free DPs A_2LiAsI_6 (A= Na, K, Cs) materials are the key characteristics for long term scalability. In all understudy materials, the alkali-metal cation (Na, K, or Cs) resides at A site of cubic DP structure (space group Fm3m, No. 225), where Li and As atoms are located at the B and B′ sites, respectively. As shown in figure 1, the iodine atoms linked in LiI_6 and AsI_6 octahedral with corner sharing thus, giving a three-dimensional framework. A highly symmetric structure is desirable for structural integrity and efficient charge transport in the halide DPs.

The Goldschmidt tolerance factor (t) was also determined for these compounds as an additional measure of geometric stability as presented in equation (7) [48].

$$t=\frac{R_A+R_X}{\sqrt{2}(R_B+R_X)} \quad (7)$$

where R_X represents the ionic radius of the anion, R_A represents the ionic radius of the larger A-site cation, and R_B represents the ionic radius of the smaller B-site cation. The computed tolerance factors of Na_2LiAsI_6, K_2LiAsI_6, and Cs_2LiAsI_6 compounds are of 0.903, 0.966, and 1.027, respectively.

The corresponding calculated values of tolerance factor (t) found within the optimal range for cubic perovskites, indicating the compounds under examination are geometrically compatible with the cubic crystal structure. The increasing trend of tolerance factor (t) with increasing A site ionic radius from Na to Cs, supports the crystal growth with enhanced structural stability for larger alkali-metal ions. The Goldschmidt tolerance factor is an empirical geometrical criterion for assessing perovskite structural suitability rather than a strict stability limit. Although Cs_2LiAsI_6 has a slightly higher value (1.027), its proximity to unity suggests compatibility with the cubic structure. This assignment is further supported by the optimized crystal geometry and mechanical stability calculations. The total energy of each compound was minimized as a function of volume of the unit cell to obtain the equilibrium structural parameters. The total energies were calculated at a sequence of compressed and expanded volumes and the Birch-Murnaghan equation (8) of state was fitted to the obtained energy-volume data [49].

$$E(V) = E_0 + \frac{9V_0B_0}{16}\left\{\left[\left(\frac{V_0}{V}\right)^{2/3} - 1\right]^3 B_0' + \left[\left(\frac{V_0}{V}\right)^{2/3} - 1\right]^2\left[6 - 4\left(\frac{V_0}{V}\right)^{2/3}\right]\right\} \quad (8)$$

where V_0 is the equilibrium unit-cell volume, B_0 is the bulk modulus, $B_{0'}$ is the pressure derivative of the bulk modulus, E(V) is the total energy at volume V, and E_0 is the minimum total energy. After the geometric optimization, the energy-volume curves of all investigated compounds are well converged, confirms the energetic stability, as displayed in figure 2(a-c).

For all compounds, the calculated lattice parameters, optimized volume, equilibrium volume, ground state energy, bulk modulus and tolerance factors are summarized in table 1. Obviously, the equilibrium volume increases from Na_2LiAsI_6 to Cs_2LiAsI_6 with increase in ionic radius of the A-site cation as $r_{Na^+} < r_{K^+} < r_{Cs}$, identify no structural deformation and retains the cubic symmetry. To further evaluate their thermodynamic stability, we calculate the formation energy of corresponding compounds using equation (9):

$$\Delta E_f = E_{tot}(A_2LiAsI_6) - [2E(A) + E(Li) + E(As) + 6E(I)] \quad (9)$$

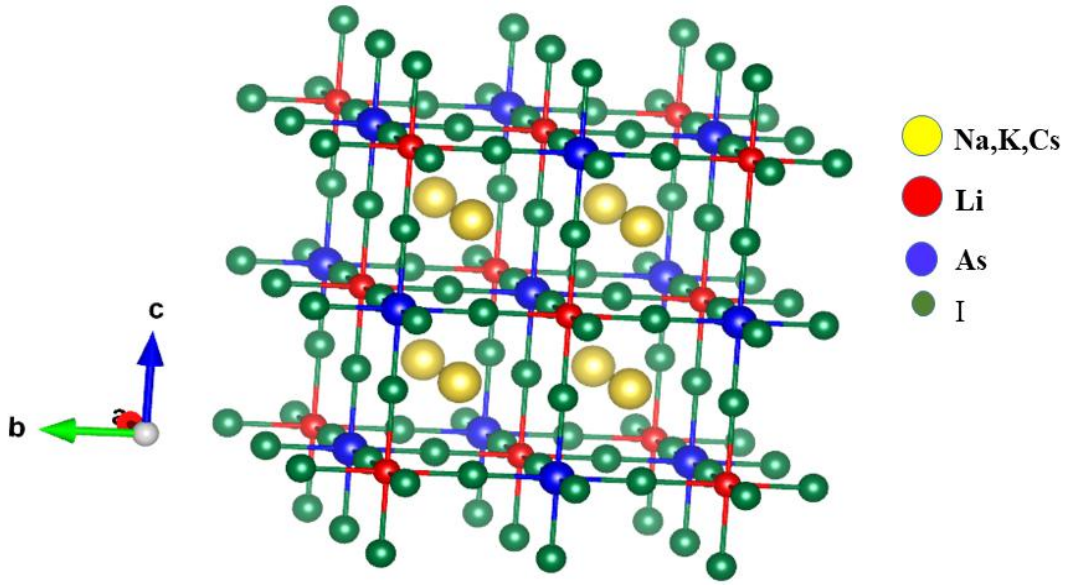

Figure 1. Crystal structure of cubic lead-free double perovskites A_2LiAsI_6 (A = Na, K, and Cs).

Where E_{tot} (A_2LiAsI_6), 2E(A), E(Li), E(As) and E(I) represent the total energy of the compound, isolated A-, Li-, As and I-atom respectively. The negative formation energies obtained for the investigated DPs compounds confirm their energetic favorability relative to the constituent elemental reference states, thereby indicating thermodynamic stability with respect to decomposition into the corresponding elemental phases [50]. Overall, these results show that A-site cation engineering can efficiently modify the structural properties of A_2LiAsI_6 DPs while maintaining the cubic symmetry. As a result, the optimized structures offer a solid foundation for comprehending the electrical, optical, elastic, and thermoelectric characteristics covered in the sections that follow.

3.2. Electronic property

To examine the electronic analysis of A_2LiAsI_6 (where A=Na, K, and Cs), we further calculated the electronic band structure along high symmetry W–L–Γ–X–W–K of first Brillouin zone and partial density of states (PDOS) using PBE-GGA and TB-mBJ approximations (Figures 3 and 4). Obviously, all the three compounds exhibit indirect semiconducting behavior with valence band maximum (VBM) located at Γ-point and conduction band minimum (CBM) positioned at L-point of the Brillouin zone. Indirect transitions generally exhibit lower optical absorption near the band edge due to the requirement for phonon assistance, which may influence solar cell efficiency. However, phonon-assisted transitions can facilitate optical absorption, and the overall photovoltaic performance also depends on other factors, including bandgap magnitude, optical absorption coefficient, and carrier transport properties.

The calculated bandgaps are 0.807 eV (Na_2LiAsI_6) and 0.812 eV (K_2LiAsI_6) and 0.873 eV (Cs_2LiAsI_6) around Fermi level (E_F = 0 eV), see table 1. Furthermore, the PBE-GGA functional underestimates the bandgap values due to improper accounting for exchange-correlation interactions. The modified Becke-Johnson potential (TB-mBJ) was employed to achieve reasonable bandgap values with more realistic electrical properties (Figure 4).

The calculated band gap of understudy compounds was listed in table 1. This trend of better bandgap with TB-mBJ approach observed in other halide DPs. In the compounds investigated Cs_2LiAsI_6 has the largest energy gap, Therefore, it is anticipated that these compounds with semiconducting behavior can be beneficial for optoelectronic applications in the visible spectrum. Figure 5 shows the total and partial densities of states (TDOS and PDOS) of A_2LiAsI_6 (A = Na, K, and Cs), which were used to identify the orbital contributions near the valence-band maximum and conduction-band minimum. I-p states dominate the valence band from −1.0 eV to the Fermi level, with substantial contributions from As-p states. The Li-s states moderately contribute to both lower valence and conduction band. In contrast, the alkali metal atoms (Na, K, and Cs) show negligible contributions near Fermi-level. However, CBM between energy range 0.0–2.0 eV is mainly contributed by As-p orbital of all compounds. Comparing the three compounds, it is seen that the replacement of Na by K and then by Cs leads to a slight change in the distribution of the electronic states and to an increase in the band gap. The larger ionic radius of Cs causes a change in the crystal field environment and interaction between the electrons, which causes greater localization of the conduction band states resulting in the highest energy gap in Cs_2LiAsI_6. Overall, the moderate indirect semiconducting band gaps suggest that these compounds have potential for optoelectronic and photovoltaic devices.

3.3. Optical properties

We calculate optical properties of A_2LiAsI_6 (A = Na, K and Cs) double perovskites to assess the optoelectronic and photovoltaic performance. The complex dielectric function, describes how electromagnetic radiation interacts with matter

[51], is given in equation (10):

$$\varepsilon(\omega) = \varepsilon_1 \quad (\omega) + i\varepsilon_2 \quad (\omega) \qquad (10)$$

The real part ($\varepsilon_1(\omega)$) shows the material capacity for polarization, whereas the imaginary part ($\varepsilon_2(\omega)$) contains contributions from optical absorption linked to interbond electronic transitions. The dielectric function's real component, $\varepsilon_1(\omega)$, calculated from the above, is shown in figure 6(a) and has positive static values for all the compounds indicating good polarizability when subjected to an external electric field. The spectra gradually increase and reach maximum values between 1.7–2.0 eV and 8.2–8.6.

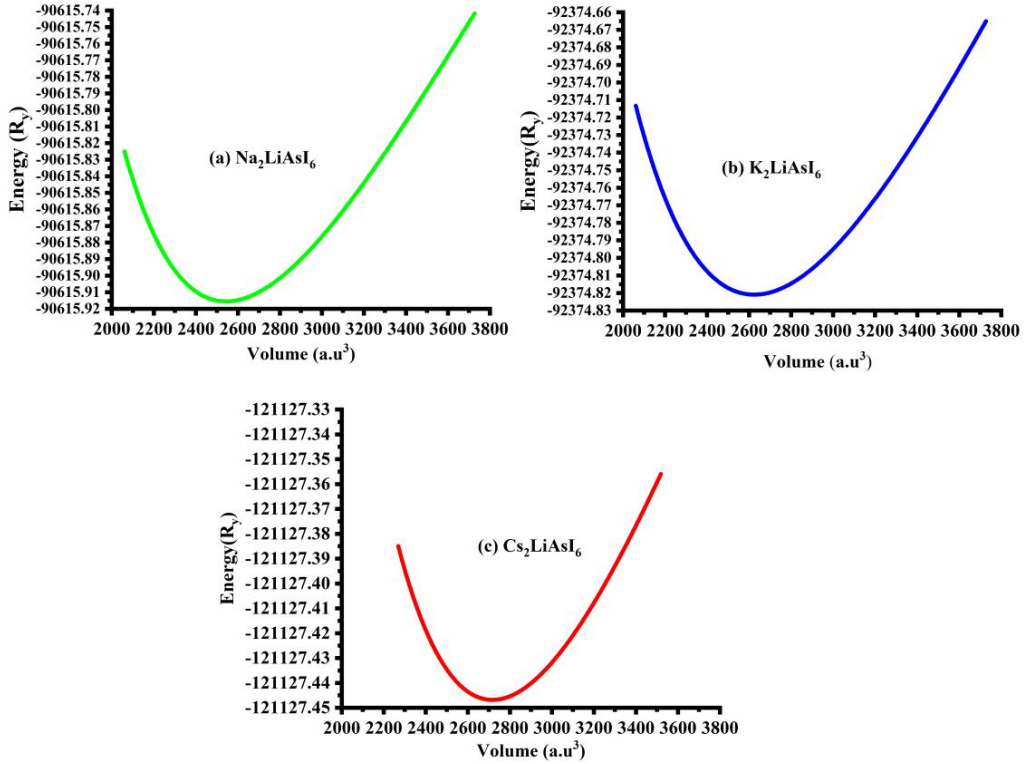

Figure 2. Energy-volume curves of A_2LiAsI_6 (A=Na, K, Cs).

Table 1. Optimized lattice constant a (Å), ground state volume (V_0, Å^3), ground-state energy (E_0, eV), bulk modulus (B_0, GPa), derivative of bulk modulus (B_0') and tolerance factor (t) and formation Energy (E_f), band gap E_g (using PBE-GGA and TB-mBJ), band gap nature of A_2LiAsI_6 (A = Na, K, and Cs) compounds.

Parameter	Na_2LiAsI_6	K_2LiAsI_6	Cs_2LiAsI_6
a (Å)	11.47	11.59	11.72
V_0 (Å^3)	2543.76	2624.05	2716.94
E_0 (eV)	−90615.92	−92374.82	−121127.45
B_0 (GPa)	19.32	17.66	17.88
B_0'	4.76	3.90	4.31
Tolerance factor (t)	0.903	0.966	1.027
E_f (eV)	-0.2194	-0.2511	-1.3664
$E_{g\text{-}GGA}$ (eV)	0.807	0.812	0.873
$E_{g\text{-}mBJ}$ (eV)	1.330	1.321	1.365
Bandgap nature	Indirect	Indirect	Indirect

Following this, it is found that the value of $\varepsilon_1(\omega)$ decreases rapidly and becomes negative near 3eV, indicating plasma-like character and the strong interaction between the incident photons and the free charge carriers. The negative values show that the electromagnetic waves in this energy range are strongly reflected. At higher energies, the peaks are broad ones between 6 and 8 eV, corresponding to transitions from occupied valence-band states to empty conduction-band states. Cs_2LiAsI_6 has slightly higher dielectric dispersion among understudy compounds, suggesting to more polarization effects. The imaginary part of dielectric function $\varepsilon_2(\omega)$ as shown in figure 6(b), demonstrate the absorption

mechanism of understudy compounds. A prominent peak with maximum intensity ~ 10.5 found at ~ 2–3 eV, is consistent with direct electronic transitions across the fundamental band gap. There are other peaks in the 7–10 eV range that are due to transitions involving hybridized As-p and I-p states. High optical activity is suggested by the wide extent of these peaks. As seen in figure 6(c), the absorption coefficient I(ω) of all the compounds has strong absorptive properties in the visible to the ultraviolet (UV) region, with the higher $\varepsilon_2(\omega)$ values for Cs_2LiAsI_6 than for Na_2LiAsI_6 and K_2LiAsI_6Very little absorption is seen at low photon energies, while very sharp absorption bands are seen between 2 and 4 eV, with the absorption being nearly 60 cm^{-1}. Absorption becomes significant at high energy level (above 6 eV) with magnitude greater than 120 cm in the ultraviolet region. For the extraction of incident photons in solar energy conversion and ultraviolet optoelectronic devices, the strong absorption characteristic would be highly helpful. greater transition probability from the valence band to the conduction band at higher energy is thought to be the cause of greater absorption. The amount of energy lost by fast electrons flow through the material is represented by the electron energy-loss function, L(ω), as shown in figure 6(d). Every compound has a noticeable peak around 3.8–4.0 eV, which is the plasma resonance frequency for the valence electrons' collective oscillations. In addition to this energy, there are several smaller peaks in the energy region (8–13 eV) and the loss function drops significantly after this energy. The highest loss peak corresponds to Cs_2LiAsI_6, which shows comparatively strong plasmonic behavior, as is shown in figure 6(c) which shows the spectra of refractive index n(ω). The static refractive indices are around 2.2–2.3, indicating high retardation of electromagnetic waves in the materials. The highest values of the refractive index are found near 1.8–2.1 eV and drop dramatically around 3 eV. There are further broad maxima at 6–8 eV, which are related to interbond electronic excitations. The refractive index tends to lower values, suggesting a less interaction between the electromagnetic radiation and the medium at higher energies. The reflectivity spectra R(ω) shown in figure 6(f) have relatively low reflectivity in the low-energy region, with the initial reflectivity being ~0.15. The reflectivity increases with the photon energy, and peaks at about 0.55–0.60. A sharp decrease is seen around 4 eV, as expected, compared to the plasma resonance frequency determined from the energy-loss spectra. The higher-energy region shows several oscillatory features, due to various interbond transitions. The moderate reflectivity and high absorption properties indicate that the photons are efficiently absorbed and there are minimal optical losses. In general, the optical properties of Na_2LiAsI_6, K_2LiAsI_6, and Cs_2LiAsI_6 suggest high dielectric response, absorption coefficient, refractive index, and reflectivity in a broad range of the optical energy spectrum. The strong absorption in the visible and UV range and the favorable dielectric and plasmonic properties suggest that these DPs are suitable for the use in photovoltaic cells, as UV photodetectors, as optical coatings and for other advanced optoelectronic applications.

3.4. Elastic properties

Elastic properties are crucial to understand the mechanical stability, stiffness, compressibility, ductility and anisotropy of crystalline solids. The total energy versus volume data were fitted to the Birch–Murnaghan equation of state to get the equilibrium structural parameters. The optimized equilibrium volumes and bulk moduli of A_2LiAsI_6 (A = Na, K, Cs) listed in table 2, identify significant difference in the compressibility of studied compounds. Specifically, Na_2LiAsI_6 and Cs_2LiAsI_6 have very small bulk moduli, indicating highly compressible and mechanically soft lattices, whereas K_2LiAsI_6 with a bulk modulus show comparatively greater resistance to compression. Similar mechanically soft behavior has been reported for other halide double perovskites [52, 53]. For cubic crystal, the elastic response is uniquely defined by three independent elastic constants: C_{11}, C_{22} and C_{44}. The bulk modulus is related to these elastic constants using the following equation (11):

$$B = \frac{C_{11}+C_{22}}{3} \qquad (11)$$

The tetragonal and rhombohedral distortions give the combinations ($C_{11}-C_{22}$) and ($C_{11} + 2C_{22} + 4C_{44}$), respectively. The calculated elastic parameters are summarized in table 2. Obviously, the calculated elastic constants obey mechanical stability condition $C_{11}-C_{22} > 0$, $C_{11} +2C_{22} > 0$, $C_{44} > 0$, confirms the mechanical stability of X_2LiAsI_6 (X = Na, K, Cs) compounds. Moreover, the positive values of C_{44} indicate resistance to shear deformation and $C_{11} > C_{22}$ reveal higher resistance to longitudinal compression along the principal crystallographic directions. The elastic anisotropy factor (A) was calculated using the following equation (12):

$$A = \frac{c_{44}}{c_{11}-c_{22}} \qquad (12)$$

where (A = 1) represents isotropic behavior. The values calculated differ significantly from one, showing that all three compounds have elastic anisotropy. The shear modulus (G) indicates the resistance to change in the shape of the material and Young's modulus (E) determine the stiffness of material. The higher values of (G) and (E) of K_2LiAsI_6 shows stronger interatomic interaction and high rigidity. However, Na_2LiAsI_6 with smaller Young's modulus indicates relatively soft nature, capable to easily stretch and bend. In addition, Poisson's ratio is an important parameter for understanding the elastic response and bonding characteristics of crystalline materials. For K_2LiAsI_6, the Poisson's ratio of 0.297 indicates a conventional elastic response with considerable resistance to shear deformation. However, the negative Poisson's ratios obtained for Na_2LiAsI_6 (-0.094) and Cs_2LiAsI_6 (−0.075) indicate unusual auxetic behavior. This behavior may be associated with the flexible nature of the crystal framework, where octahedral tilting, bond-angle variations, and cooperative lattice deformations may facilitate lateral expansion during stretching. Such structural flexibility may contribute to the unusual elastic response of these compounds.

Using Pugh's criterion, the brittle or ductile nature of understudy materials were examined. Based on this criterion, a material is classified as ductile if:

$$\frac{B}{G} > 1.75 \qquad (13)$$

The calculated (B/G) ratios suggest that K_2LiAsI_6 is ductile with the ratio of 2.13 however, Na_2LiAsI_6 and Cs_2LiAsI_6 with (B/G) ratio less than 1.75 exhibit brittle nature. Increased ductility of K_2LiAsI_6 is beneficial for thin film and flexible device applications. Overall, K_2LiAsI_6 reveal higher stiffness, greater resistance to compression and ductile nature, making it as promising candidate with higher mechanical flexibility for optoelectronic devices and photovoltaics.

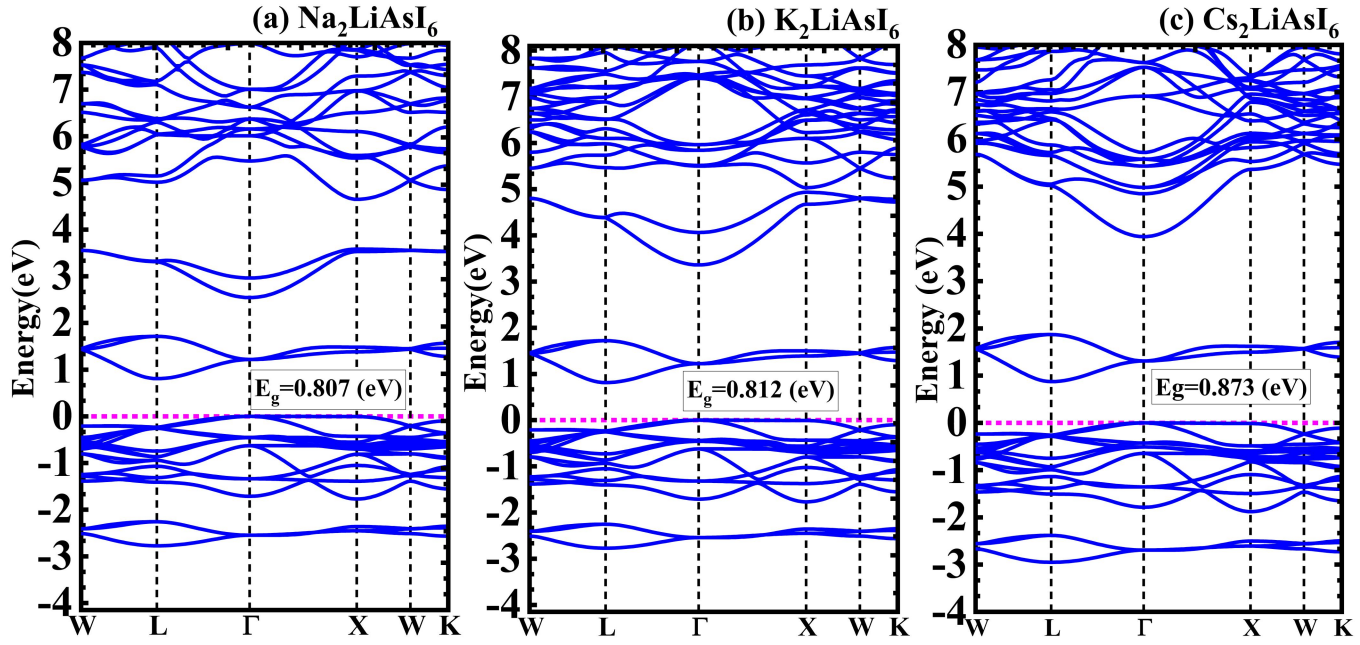

Figure 3. Calculated electronic band structures of A_2LiAsI_6 (Na, K, Cs) using GGA methods.

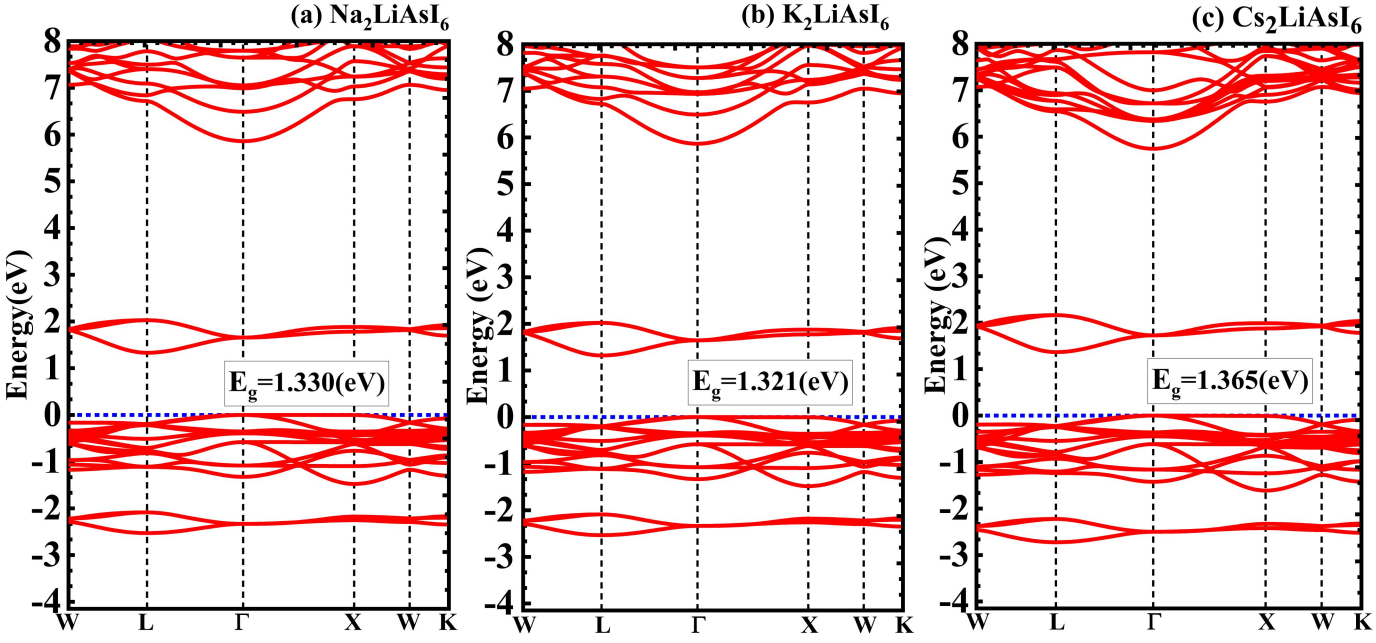

Figure 4. Calculated electronic band structures of A_2LiAsI_6 (Na, K, Cs) using TB-mBJ methods.

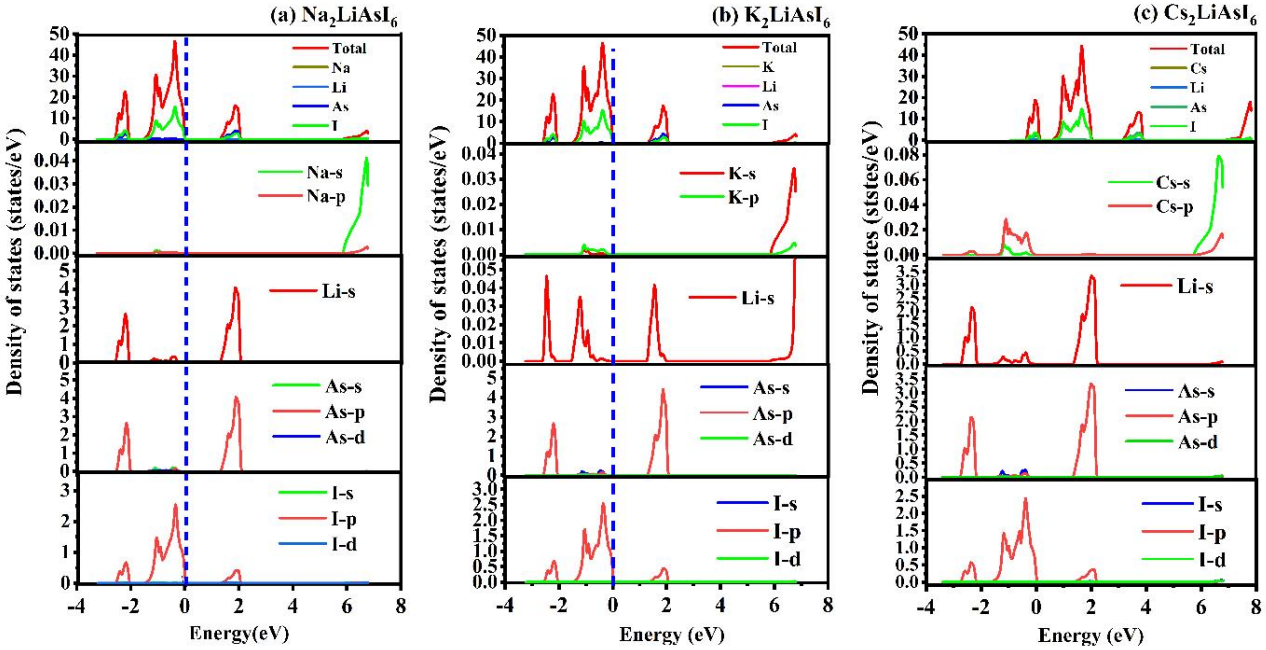

Figure 5. Total and partial density of states (TDOS and PDOS) of A_2LiAsI_6 (A=Na, K, Cs).

3.5. Thermoelectric property

Next, we examine the transport coefficient of $A_2LiAsI6$ (Na, K, Cs) compounds using semi-classical Boltzmann transport theory implemented in Boltz Trap code. The calculated Seebeck coefficient (S), electrical conductivity (σ), power factor (PF), and heat capacity (C_V) versus temperature are displayed in figure 7(a–d) [54]. It is evidently clear from figure 7(a) that Seebeck coefficient decreases with increase in temperature. At 50 K, 2.67×10^{-4} V/K of Na_2LiAsI_6 exhibit found values are approximately 2.08×10^{-4} V/K and 2.20×10^{-4} V/K for K_2LiAsI_6 and Cs_2LiAsI_6, respectively [55, 56]. At 800 K, the Seebeck coefficients decrease to nearly 1.84×10^{-4}, 1.80×10^{-4} and 1.86×10^{-4} V/K for Na_2LiAsI_6, K_2LiAsI_6, and Cs_2LiAsI_6, accordingly. This decrease is due to the improved thermal excitation, and the elevated temperature increase in the number of carriers. With a higher concentration of thermally generated carriers, the thermoelectric voltage across the material is decreased, in general, because the Seebeck coefficient is inversely proportional to carrier concentration. The positive values of S in the whole investigated temperature range are a confirmation of the p-type semiconducting nature of these compounds. The Seebeck coefficient (S) is defined by the following equation (14):

$$S = \frac{-\Delta V}{\Delta T} \qquad (14)$$

The temperature dependence of electrical conductivity split by relaxation time (σ/τ) is shown in figure 7(b). The electrical conductivity of all investigated compounds increases monotonically with increasing temperature, indicating their semiconducting behavior. At 50 K, the conductivity values are close to $0.4\times10^{11}\Omega^{-1}m^{-1}s^{-1}$ and increase continuously up to approximately 3.95×10^{11}, $4.02\times10^{11}$and $4.30\times10^{11}\Omega^{-1}m^{-1}s^{-1}$ at 800 K for Na_2LiAsI_6 K_2LiAsI_6 and Cs_2LiAsI_6, respectively. The higher mobility of the carriers and the increased orbital overlap caused by the larger lithium-ion size could be responsible for the higher conductivity of Cs_2LiAsI_6, compared to Cs_2LiAsI_6, Thermal activation of electrons, coupled to an increase in the number of charge carriers, is responsible for the rise in electrical conductivity with temperature. The electrical conductivity (σ) is expressed by the following equation (15):

$$\sigma = ne\mu \qquad (15)$$

where ne and μ stand for carrier concentration, electron charge, and carrier mobility, respectively.

The temperature dependence of the power factor (PF) is presented in figure 7(c), reflected that the PF increases nearly linearly with the temperature for all the compounds. At 50 K, PF values are close to 1.0×10^{18} WK^{-2} ms, and rise continuously to approximately 1.18×10^{19}, 1.22×10^{19} and 1.25×10^{19} WK^{-2} ms at 800 K for Na_2LiAsI_6, K_2LiAsI_6, and Cs_2LiAsI_6, respectively. The Seebeck coefficient will decrease with increasing temperature, but the large increase in electrical conductivity will offset this effect, resulting in an overall improvement of PF. The investigated compounds Cs_2LiAsI_6 has the highest power factor and thus has the best electrical power generation properties. The power factor (PF) is calculated using the following equation (16):

$$PF = S^2\sigma \qquad (16)$$

The relationship between temperature and heat capacity at constant volume (Cv) is depicted in figure 7(d). It is well known that an increase in temperature causes the heat capacity to rise., so that the latter grows monotonically with the increase of temperature, due to the gradual excitation of

phonon modes and the growing degree of lattice vibrations. The heat capacities are roughly 1 $Jmol^{-1}K^{-1}$ at 50 K but rise to ~25.5, 25.8 and 22.0 $Jmol^{-1}$ K^{-1} for Na_2LiAsI_6, K_2LiAsI_6, and Cs_2LiAsI_6, respectively, at 800 K. The values of heat capacity of K_2LiAsI_6 are largest and Cs_2LiAsI_6 have comparatively smaller values within the range of temperatures considered.

Table 2. Calculated elastic constants and mechanical parameters of $A_2LiAsI6$ (A=Na, K, Cs)

Parameter	Na_2LiAsI_6	K_2LiAsI_6	Cs_2LiAsI_6
Equilibrium volume ($bohr^3$)	3587.99	2199.09	3414.38
C_{11} (GPa)	4.279	79.023	14.374
C_{22} (GPa)	0.325	20.674	-0.133
C_{44} (GPa)	4.501	13.952	9.950
Bulk modulus (B) (GPa)	1.643	40.124	4.703
Shear modulus (G) (GPa)	3.325	18.836	8.767
Young's modulus (E) (GPa)	5.860	48.863	16.221
Poisson's ratio (ν)	-0.094	0.297	-0.075
Anisotropy factor (A)	2.276	0.478	1.372
(B/G) ratio	0.508	2.130	0.536
Mechanical nature	Brittle	Ductile	Brittle

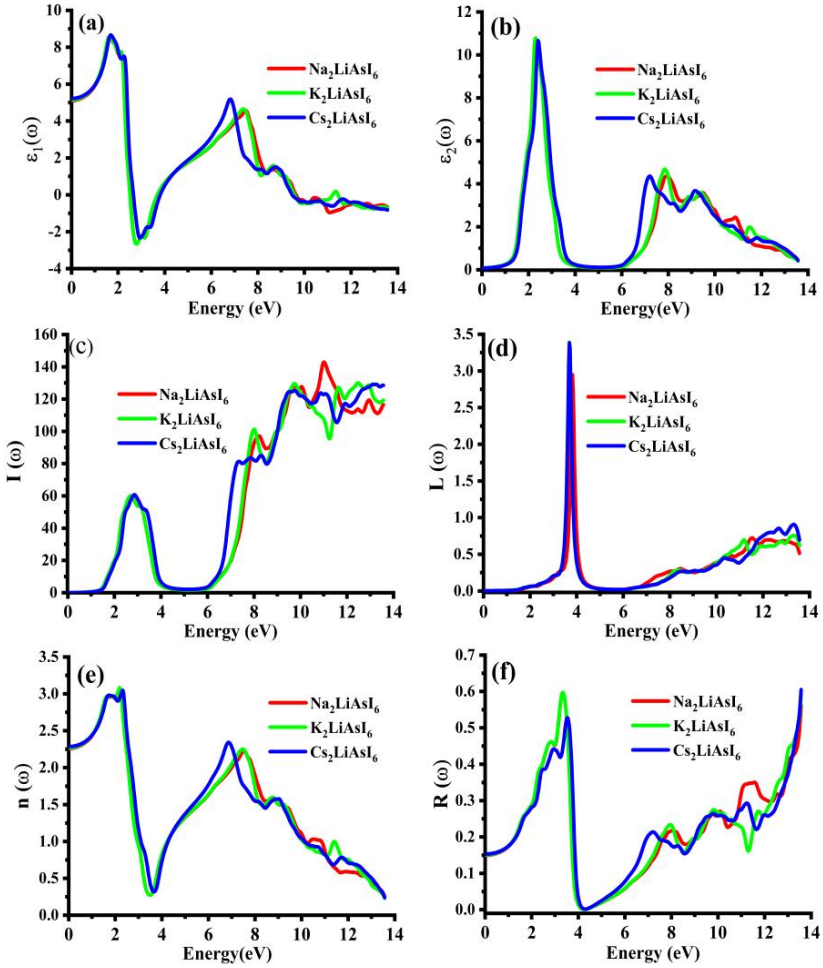

Figure 6. calculated optical properties of A_2LiAsI_6 (A = Na, K, and Cs) (a) real dielectric function, (b) imaginary dielectric function (c) absorption coefficient (d) energy-loss function (e) refractive index (f) reflectivity.

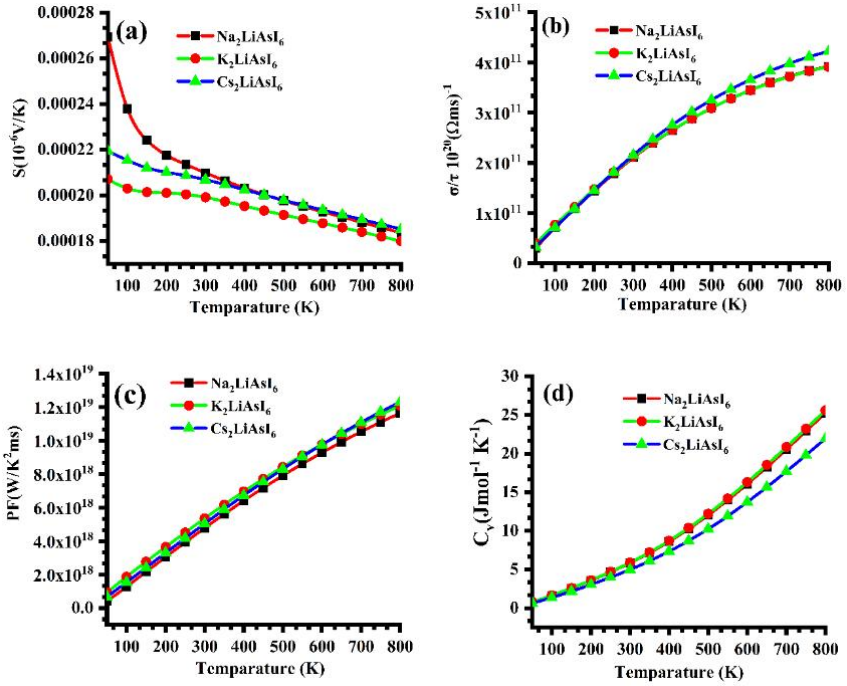

Figure 7. Temperature-dependent (a) Seebeck coefficient, (b) electrical conductivity, (c) power factor, and (d) heat capacity of A_2LiAsI_6 (A = Na, K, and Cs).

The gradual increase of heat capacity is taken as evidence of good thermal stability and absence of any structural phase transition in the temperature range of consideration. The heat capacity at constant volume (Cv) is defined by the equation (17):

$$C_v = \left(\frac{\partial U}{\partial T}\right)_v \qquad (17)$$

On the whole, the thermoelectric transport properties suggest that Na_2LiAsI_6, K_2LiAsI_6 and Cs_2LiAsI_6 are good candidates for thermoelectric energy conversion. for a high and medium temperatures, these materials promising candidates for thermoelectric applications because of their relatively high Seebeck coefficients and increase in electrical conductivity, power factor increasing with increasing temperature. Specifically, Cs_2LiAsI_6 has excellent electrical conductivity and high-power factor, highlighting it a desirable material for waste-heat recovery and renewable energy devices.

4. Conclusion

The DFT within the framework of FP-LAPW was used to investigate the lead-free halide DPs A_2LiAsI_6 (A = Na, K, and Cs). The positive tolerance factors and negative formation energies confirm the geometric and thermodynamic stability. As the A-site ionic radius increases, the lattice constant and equilibrium volume gradually increase, demonstrating that cation substitution is a useful technique for regulating these materials structural characteristics. All compounds are indirect semiconductors with bandgap ranging from 1.321 to 1.365 eV, suitable for visible-light harvesting. The mechanical analysis showed that all the compounds meet the Born stability criteria for cubic crystals. Among all, K_2LiAsI_6 possess highest stiffness and ductility nature. Notably, the Seebeck coefficient decreases with increase in temperature while the electrical conductivity and power factor increases with the temperature. Moreover, C_2LiAsI_6 shows good thermoelectric performance as compared to Na_2LiAsI_6 and K_2LiAsI_6. The present work reveals that the A-site cation engineering significantly affects the optoelectronic and thermoelectric properties of A_2LiAsI_6 DPs, making them appealing multifunctional materials for next-generation photovoltaic, optoelectronic, and thermoelectric energy-conversion technologies.

Author contributions

Masaood Khan: Conceptualization, Methodology, Software, Investigation, Writing–original draft. Murad Khan: Conceptualization, Methodology, Software, Investigation, Writing–original draft. Khalid Khan: Formal analysis, Data curation, Visualization. Muhammad Khurshid: Validation, Formal analysis, Visualization. Muhammad Jamshed: Supervision, Project administration, Writing–review & editing. Zama Jan: Supervision, Project administration, Writing–review & editing. All authors have read and agreed to the published version of the manuscript.

Ethical approval

Not applicable. This study did not involve any human or

animal subjects.

Conflicts of Interest

The authors declare that they have no known competing financial interests or personal relationships that could have appeared to influence the work reported in this paper.

Acknowledgment

The authors would like to express their sincere gratitude to Abdul Wali Khan University (Pakistan), Xi'an Jiaotong University and Hainan Normal University (China) for providing the necessary computational resources, software, and research facilities that made this work possible. This research did not receive any specific grant from funding agencies in the public, commercial, or not-for-profit sectors.

Data availability statement

The data that support the findings of this study are available from the corresponding author upon reasonable request.

Funding

The authors received no financial support for the research, authorship, and/or publication of this article.

REFERENCES

1. Weeks, C. and M. Franz, Topological insulators on the Lieb and perovskite lattices. Physical Review B—Condensed Matter and Materials Physics, 2010. 82(8): p. 085310.
2. Sofi, M.Y. and D.C. Gupta, Scrutinized the inherent spin half-metallicity and thermoelectric response of f-electron-based RbMO3 (M= Np, Pu) perovskites: a computational assessment. Scientific Reports, 2022. 12(1): p. 19476.
3. Yu, X., et al., Recent progress in modular electrochemical synthesis of hydrogen and high-value-added chemicals based on solid redox mediator. Small, 2025. 21(28): p. 2310573.
4. Berri, S., First-principles calculations to investigate structural, electronic, elastic, optical and transport properties of halide double perovskites Cs2ABF6 (AB= BiAu, AgIr, CuBi, GaAu, InAs, InAg, InAu, InSb and InBi) for solar cells and renewable energy applications. Chemical Physics Letters, 2023. 826: p. 140653.
5. Li, J., et al., Recent advances in scanning electrochemical microscopy for probing the sites in electrocatalysts. Journal of Materials Chemistry A, 2024. 12(30): p. 18733-18750.
6. Jamesh, M.-I., et al., Advancement of technology towards developing perovskite-based solar cells for renewable energy harvesting and energy transformation applications. npj Materials Sustainability, 2025. 3(1): p. 29.
7. Ali, M., et al., CO Adsorption on two-dimensional 2H-ZrO2 and its effect on the interfacial electronic properties: implications for sensing. Physica Scripta, 2023. 98(11): p. 115801.
8. Jan, Z., et al., First-principles study of strain and electric field tuning of the electronic structure and thermoelectric response in LiXYO6 double perovskites (X= Nb, ta; Y= Mo, W). Computational Materials Science, 2026. 268: p. 114670.
9. Saidi, S., et al., First-principles study of electronic, optical, and transport characteristics of double perovskites Tl2XI6 (X= Se, Te) for renewable energy applications. Journal of Physics and Chemistry of Solids, 2025: p. 113247.
10. Deligoz, E., et al., Lead-free Na2ZrTeO6 double perovskite: a promising candidate for high-temperature and optoelectronic applications. Advanced Theory and Simulations, 2025. 8(6): p. 2401421.
11. Yi, C., et al., Perovskite Photovoltaics with Outstanding Performance Produced by Chemical Conversion of Bilayer Mesostructured Lead Halide/TiO2 Films. Advanced materials (Deerfield Beach, Fla.), 2016. 28(15): p. 2964-2970.
12. Yin, G., et al., Precursor engineering for all-inorganic CsPbI2Br perovskite solar cells with 14.78% efficiency. Advanced functional materials, 2018. 28(39): p. 1803269.
13. Sutton, R.J., et al., Bandgap-tunable cesium lead halide perovskites with high thermal stability for efficient solar cells. Advanced Energy Materials, 2016. 6(8): p. 1502458.
14. Yang, W.S., et al., High-performance photovoltaic perovskite layers fabricated through intramolecular exchange. Science, 2015. 348(6240): p. 1234-1237.
15. Chen, X., et al., Bayesian optimization based on a unified figure of merit for accelerated materials screening: A case study of halide perovskites. Science China Materials, 2020. 63(6): p. 1024-1035.
16. Slavney, A.H., et al., A bismuth-halide double perovskite with long carrier recombination lifetime for photovoltaic applications. Journal of the American chemical society, 2016. 138(7): p. 2138-2141.
17. McClure, E.T., et al., Cs2AgBiX6 (X= Br, Cl): new visible light absorbing, lead-free halide perovskite semiconductors. Chemistry of Materials, 2016. 28(5): p. 1348-1354.
18. Wang, G., et al., Mechanical chameleon through dynamic real-time plasmonic tuning. ACS nano, 2016. 10(2): p. 1788-1794.
19. Volonakis, G., et al., Cs2InAgCl6: a new lead-free halide double perovskite with direct band gap. The journal of physical chemistry letters, 2017. 8(4): p. 772-778.
20. Liu, X., J. Gao, and Q. Wang, Structural-property correlations of all-inorganic CsPbBr3 perovskites via synergetic controls by PbBr2, 2-mercapto-3-methyl-4-thiazoleacetic acid and water. Chemical Engineering Journal, 2022. 428: p. 131117.
21. Babayigit, A., et al., Toxicity of organometal halide perovskite solar cells. Nature materials, 2016. 15(3): p. 247-251.
22. Tiong, V.T., et al., Octadecylamine-functionalized single-walled carbon nanotubes for facilitating the formation of a monolithic perovskite layer and stable solar cells. Advanced Functional Materials, 2018. 28(10): p. 1705545.
23. López-Fernández, I., et al., Lead-free halide perovskite materials and optoelectronic devices: progress and prospective. Advanced Functional Materials, 2024. 34(6): p. 2307896.
24. Murtaza, G., et al., Lead free double perovsites halides X2AgTlCl6 (X= Rb, Cs) for solar cells and renewable energy applications. Journal of Solid State Chemistry, 2021. 297: p. 121988.
25. Ma, X., Z. Li, and J. Yang, Efficient direct band gap photovoltaic material predicted via doping double perovskites Cs2AgBiX6 (X= Cl, Br). The Journal of Physical Chemistry C, 2021. 125(20): p. 10868-10875.
26. Volonakis, G., et al., Lead-free halide double perovskites via heterovalent substitution of noble metals. The journal of physical chemistry letters, 2016. 7(7): p. 1254-1259.
27. Tailor, N.K., et al., Lead-free halide double perovskites: fundamentals, challenges, and photovoltaics applications. Advanced Materials Technologies, 2023. 8(1): p. 2200442.
28. Chen, H., et al., Optoelectronic properties of Rb-doped inorganic double perovskite Cs2AgBiBr6. Chemical Physics Letters, 2021. 771: p. 138501.
29. Sa, R., et al., A first-principle study of the structural, mechanical, electronic and optical properties of vacancy-

ordered double perovskite Cs2TeX6 (X= Cl, Br, I). Chemical Physics Letters, 2020. 754: p. 137538.
30. Yu, L., et al., A comprehensive review of fluorescence correlation spectroscopy. Frontiers in physics, 2021. 9: p. 644450.
31. Obada, D.O., et al., Lead-free double perovskites: a review of the structural, optoelectronic, mechanical, and thermoelectric properties derived from first-principles calculations, and materials design applicable for pedagogical purposes. Crystals, 2024. 14(1): p. 86.
32. Zhou, H., et al., Flotation behavior and mechanism of smithsonite under the system of bidentate ligand sulfide sodium thiocyanate. Separation and Purification Technology, 2024. 334: p. 126086.
33. Bhamu, K., A. Soni, and J. Sahariya, Revealing optoelectronic and transport properties of potential perovskites Cs2PdX6 (X= Cl, Br): a probe from density functional theory (DFT). Solar Energy, 2018. 162: p. 336-343.
34. Zhou, H., et al., Highly efficient preparation of crystalline yttrium carbonate in sodium carbonate system: Formation and growth mechanism. Journal of Rare Earths, 2025. 43(7): p. 1492-1501.
35. Zhang, T., C. Hu, and S. Yang, Ion migration: a "double-edged sword" for halide-perovskite-based electronic devices. Small Methods, 2020. 4(5): p. 1900552.
36. Meng, W., et al., Parity-forbidden transitions and their impact on the optical absorption properties of lead-free metal halide perovskites and double perovskites. The journal of physical chemistry letters, 2017. 8(13): p. 2999-3007.
37. Sofi, S.A. and D.C. Gupta, Current research and future prospective of cobalt-based Heusler alloys as thermoelectric materials: A density functional approach. International Journal of Energy Research, 2021. 45(3): p. 4652-4668.
38. Haque, E. and M.A. Hossain, Electronic, phonon transport and thermoelectric properties of Cs2InAgCl6 from first-principles study. Computational Condensed Matter, 2019. 19: p. e00374.
39. Zhao, X.-G., et al., Design of lead-free inorganic halide perovskites for solar cells via cation-transmutation. Journal of the American Chemical Society, 2017. 139(7): p. 2630-2638.
40. Mathew, N.P., N.R. Kumar, and R. Radhakrishnan, First principle study of the structural and optoelectronic properties of direct bandgap double perovskite Cs2AgInCl6. Materials today: proceedings, 2020. 33: p. 1252-1256.
41. Kumar, N.R. and R. Radhakrishnan, Electronic, optical and mechanical properties of lead-free halide double perovskites using first-principles density functional theory. Materials Letters, 2018. 227: p. 289-291.
42. Zhao, S., et al., First-principles study of electronic and optical properties of lead-free double perovskites Cs2NaBX6 (B= Sb, Bi; X= Cl, Br, I). Journal of Physics and Chemistry of Solids, 2018. 117: p. 117-121.
43. Schwarz, K., P. Blaha, and G.K. Madsen, Electronic structure calculations of solids using the WIEN2k package for material sciences. Computer physics communications, 2002. 147(1-2): p. 71-76.
44. Andersen, O.K., Linear methods in band theory. Physical Review B, 1975. 12(8): p. 3060.
45. Dar, S.A., et al., Investigation on the electronic structure, optical, elastic, mechanical, thermodynamic and thermoelectric properties of wide band gap semiconductor double perovskite Ba2InTaO6. RSC advances, 2019. 9(17): p. 9522-9532.
46. Usman, T., et al., Tailoring halide double perovskite materials Rb2MgSnY6 (Y= I, Br, Cl) for enhanced optoelectronic and solar cells through first-principles study. Opto-Electronics Review, 2025: p. e155902-e155902.
47. Shah, S., et al., Electronic structure, optical and magnetic properties of double Perovskites La2MTiO6 (M= Co, Ni, Cu and Zn). Materials Chemistry and Physics, 2021. 272: p. 125050.
48. Saeed, M., et al., Optoelectronic and elastic properties of metal halides double perovskites Cs_2InBiX_6 (X?=? F, Cl, Br, I). Chinese Optics Letters, 2021. 19(3): p. 030004.
49. Marcondes, M.L. and R.M. Wentzcovitch, Hybrid ab-initio/experimental high temperature equations of state: Application to the NaCl pressure scale. Journal of Applied Physics, 2015. 117(21).
50. Yu, C.-J., et al., First-principles study on structural, electronic and optical properties of halide double perovskite Cs2AgBX6 (B= In, Sb; X= F, Cl, Br, I). RSC advances, 2023. 13(23): p. 16012-16022.
51. Yaqoob, A., et al., A theoretical study for investigation of structural, optical, electronic, and mechanical properties of double perovskites halide for solar cell application. Conclusions in Engineering, 2025. 1(2): p. 72-81.
52. Dai, Z., et al., The mechanical behavior of metal-halide perovskites: Elasticity, plasticity, fracture, and creep. Scripta Materialia, 2023. 223: p. 115064.
53. Shakeel, S., et al., DFT analysis of elastic and optoelectronic properties of Cs2NaXCl6 (X= In, La, Sc, Y) double perovskite compounds. Materials Chemistry and Physics, 2024. 324: p. 129683.
54. Cappai, A., C. Melis, and L. Colombo, Role of electron-phonon scattering on thermoelectric coefficients in pristine Cs 2 NaYbCl 6 perovskite: A full DFT approach. Physical Review Materials, 2025. 9(5): p. 054605.
55. Dalbanbay, A., et al., A Computational Study of the Structural, Optoelectronic, and Thermoelectric Properties of Rb2BiAuX6 (X= Cl, Br) Halide Double Perovskites. Energy Technology, 2025. 13(12): p. 2501280.
56. Javed, A., et al., Tuning the structural, optoelectronic, and thermoelectric performance of cesium based double perovskite halide under hydrostatic pressure. Discover Nano, 2026. 21(1): p. 436.

How to cite this article:
Khan, M., Khan, M., Khan, K., Khurshid, M., Jamshed, M., & Jan, Z. (2026). Theoretical Insights into Optoelectronic and Thermoelectric Response of A_2LiAsI_6 (A = Na, K, Cs) Double Perovskite. Journal of Chemistry and Environment, 5(2), 47-58.

Copyright © 2026 by the author(s).
Published by Science Research Publishers.
This article is an open-access article distributed under the terms and conditions of the Creative Commons Attribution-NonCommercial-NoDerivatives (CC BY-NC-ND 4.0) License
Visit https://creativecommons.org/licenses/by-nc-nd/4.0/